 DOI: 10.3217/978-3-85125-869-1-04

High-Speed Stereoscopic Fragment Tracking in Industrial Filter Cleaning

Friedrich Holzinger[1], Michael Schneeberger[2], Manfred Klopschitz[2], Martina Uray[2], Matthias Rüther[1] and Gernot Krammer[1]

***Abstract*— Dust filtration is a critical operation in industrial processes, especially for environmental gas cleaning. Thereby, contaminated gas is passed through a fabric that holds back solid particles. Over time, these particles form a compact layer on the fabric surface further denoted as filter cake. This filter cake is periodically cleaned off via reverse air jet pulses, which cause an explosive breakup of the cake. To gather insights on the mechanics of this breakup, a high-speed, contactless 3D-monitoring method is presented and evaluated on laboratory scale. Results show that, despite the untextured appearance of the filter cake, for the first time a continuous three-dimensional evaluation of the filter cake motion is made possible. From our experiments, a novel data set is provided which will allow the derivation of mechanical parameters for filter cake fragments and allow the implementation and validation of dynamic simulations further on.**

I. INTRODUCTION

Industrial filter systems typically are implemented as bag-houses, i.e. batteries of hanging, cylindrical filter bodies which receive contaminated gas on the outside and deliver cleaned gas on the inside of each cylinder. They are applied in processes like waste compustion to reduce the emission of solid particles. In this process a permeable filter medium in the gas stream blocks particles up to $10\times$ smaller than its pore diameter, from passing through. As a consequence, dust particles deposit on the filter surface and form a powdery layer, which is commonly denoted as filter cake. Over time, the layer thickness increases and with it also the flow resistance. To ensure a continuous process, it is mandatory to remove the filter cake after a certain time or pressure limit. This is often accomplished by a reverse jet pulse of compressed air of about 100 milliseconds, which is applied in opposite gas flow direction and pushes the filter cake off the filter surface. It is common practice that the pulse is applied in-situ, without the interruption of filtration. This combination of a continuous forward air flow and a reverse air pulse creates a complex breakup scenario of filter cake with fragments partially flying off the filter surface, dispersing or being reattached. In this work, filter cleaning scenarios are reproduced at laboratory scale and a computer vision system is presented, which allows to observe the cleaning process at high temporal resolution. A considerable challenge is the 3D tracking of the decomposing filter cake components, despite the white, untextured surface, the high speed of motion and the continuous decomposition of the components. We thereby introduce a semi-automated approach, where a high-speed stereoscopic camera-projector-system is used to generate a sequence of depth maps, followed by manual annotation of particle agglomerates.

*This work was supported by the Austrian Science Fund (FWF) grant no. P30447-N32. Thanks to the Institute of Computer Graphics and Vision of the TUG for providing parts of the equipment.

[1]TUG - Institute of Process and Particle Engineering friedrich.holzinger@student.tugraz.at, krammer@tugraz.at

[2]JOANNEUM RESEARCH Forschungsgesellschaft mbH - DIGITAL name.surname@joanneum.at

A. Background of Optical Instruments in the Field of Filtration

In releated work, 2D image sensors were used to observe the partial removal of dust from filters [6] (p. 213), [4]. Usually, one camera scanned one section after another and 3D data allowed a quasi-static layer height analysis. This data was obtained with a single camera e.g., by directing structured light patterns on the surface [2]. Other groups demonstrated the benefits of using a stereo camera among other imaging techniques [8], [7] as usually perfect alignment of the equipment is not required, and a single shot is recorded in a short period of time enabling real-time applications. In this work the high-speed stereo camera provides time-resolved 3D images for above analysis of the course of patches that liberated from the filter during the cleaning pulse.

II. OPTICAL SYSTEM INTEGRATION

In order to reproduce a filter cleaning process at laboratory scale, first the minimum required filter area must be determined, which has to be used in a lab test in order to produce representative results. In a production environment, industrial filter material is always spanned over a grid of support rods. The grid size ultimately determines the size of a laboratory setup, because it defines an isolated cell of filter operation and a scallopping of the filter material is confined by the supporting rods. This grid size is reported to be in the range of 30 to 40 *mm* in width and 200 to 400 *mm* in length. As the scalloping effect is evident circumferentially, the width of the grid is the limiting dimension for lab scale reproduction. At the lab-scale rig, this dimension is reflected in the 70 *mm* diameter of the filter fixation ring, which is inserted between a cylinder and a pressing ring. The test rig is designed to operate at normative test conditions standardized in ISO 11057, therefore the ring orifice makes 56 *mm* of the filter visible. Particulate gas is fed directly towards the filter via a diffusor outlet. Downstream, the cylinder is connected to a blower that ensures a forced direction of flow. The

dust-containing volume between raw gas outlet and filter is confined by a metallic chamber that allows the obeservation by an optical system from the outside. The construction dimensions are shown on the sketch on the left half of Figure 1. A side channel is used to further reduce the minimum gas flow rate, resulting in a filtration speed of about 20 m/min. The intended measurement volume of the vision system is given by a cylinder with the filter surface at the bottom and a height of 20 *mm*. The cameras are situated opposite the filter, where a 6 *mm* thick composite glass replaces the metallic wall to allow optical access and still prevent the optical system from dust deposits. The glass can be cleaned by a magnetic wiper, inside from the outside. As shown in the photograph on the right half of Figure 1, the optical system consists of two synchronized cameras, capturing images in 512 *px* x 600 *px* resolution at a framerate of 500 *Hz*. Due to the high motion speed, the camera exposure is set to a maximum of 750 μs and synchronized to a high-power LED flashlight. To assist an automated dense stereo reconstruction, the directed LED illumination is enhanced by a static random dot pattern, generated by a Laser light source. In this combination, the directed LED light generally generates crisp shadows at filter cake cracks and edges, while the random dot pattern generates a dense surface texture. In this way, the conditions at the onset of the cleaning pulse can be examined, which reaches a steady state after about 20 *ms*. The acquisition of an image sequence is triggered by the pressure valve of the reverse jet pulse. The optical distance of the cameras, both focused on the center point of the top filter surface, is about 374 *mm* – each with a stereo angle of about 15° giving a stereo base (the distance of the optical lenses) of about 100 *mm*.

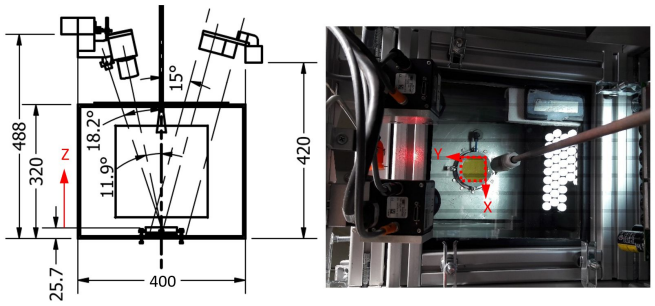

Fig. 1. Left: Sketch of test rig in front view with outlined metallic box. Right: Photograph of test rig from top. From left to right: pattern generator, stereo camera, filter fixed in holder, powder feed with diffusor, magnetic wiper (top corner) and lighting system. Viewed window (dashed red). Z direction (left) and X, Y direction (right). Dimensions in *mm*.

Due to restrictions in camera resolution at the respective speed, the cameras observe the active area of the filter medium over a window of 45×53 *mm* with a resolution of $86-90$ $\mu m/px$. In Subsection IV-A the confidence interval for depth values is found to be 94 μm. The stereo-optic method would be able to resolve in the range of the pixel resolution, provided that the distance of all points on the surface can be detected correctly.

III. Methods and Procedures

Once the setup is configured, images from both cameras can be captured. To obtain 3D information of the observed patch surfaces based on their distances to the filter, several post-processing steps are required. The filter will be removed after an experiment and may bend during an experiment but will maintain its position at the circumference once clamped in the holder and tightened. Therefore, calibration is required prior to an experiment. Here the applied methods are introduced in their experimental sequence.

A. Calibration

After the insertion of a clean filter medium sample, the camera system is calibrated by a planar calibration target with randomized dot pattern [10] [5]. Prior to filtration or cleaning one snapshot should contain the fixed filter with the pressing ring. The reason is given in Subsection III-C for the sake of operating sequence using the stereo-optical system.

B. Stereo-Matching

The goal of stereo-matching is to obtain a temporal sequence of depth maps in the stereo coordinate frame. The depthmaps need to be dense while conserving edges as good as possible. A specific challenge in the matching problem is the uncommon type of scenery, on which more recent learning-based stereo matching algorithms give worse results than traditional algorithms. Moreover, the pure white powder completely lacks texture, as does the background of the flying fragments, which is due to the directional illumination. For foreground fragments, this problem is mitigated by projecting a random dot pattern on the surface, but the background still remains dark and untextured. Therefore, any dense stereo matching algorithm will extrapolate the disparity information obtained at nearby fragment edges,thus reporting excessively high disparity in these regions. Adding a verification step through forward-backward matching helps to identify these regions, but nonetheless the fragment edges are not depicted sharply in the disparity map. After a qualitative comparison of recent stereo matching algorithms to traditional ones [3], we chose to apply a modified version of the well established semi-global matching algorithm (SGM) to compute the disparity map. A synchronized camera pair delivers images at a rate of 500 Hz. In contrast to the original SGM implementation, our algorithm is completely based on floating-point operations without performance loss and uses an M-Census metric for matching and bilateral filtering. To increase the overall accuracy, subpixel matching is performed over the entire image pyramid. Especially for planar, oblique objects like filter cake fragments, a slanted window matching is applied to compensate for perspective distortions. The obtained disparity information is converted to metric space with X and Y coordinates parallel to the primary camera's image plane and the Z coordinate towards the filter surface along the camera's principal direction. Figure 2 shows the result of two disparity map computations. A state of the art machine-learning-based method [9] (left) has a tendency

to hallucinate depths and does not give a clear distinction between individual patches. A modified SGM method with forward-backward-matching creates more sparse, but also more reliable 3D measurements.

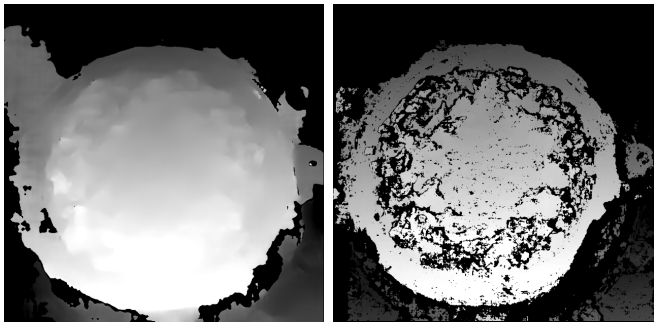

Fig. 2. Disparity map comparison of a machine-learning based stereo matching algorithm [9] (left) and a modified SGM algorithm (right).

C. Coordinate Transform Using Markers

The exact mounting position of the filter under test relative to the stereo setup may vary between experiments. In order to make these experiments comparable, a camera pose-independent coordinate system has to be defined and each experiment needs to be referenced to it. This reference coordinate system was defined relative to the mounting ring of the filter surface and is therefore as close as possible to the filter under test. Dedicated reference points with known world coordinates are marked on the fastening rings as shown in Figure 3, detected in the stereo images, refined to subpixel accuracy and finally triangulated. A rigid registration step transforms the measurement coordinate frame into the reference world frame. The resulting reference world frame is parallel to the filter plane with the perpendicular Z coordinate directing to the cameras and the origin at the center of the filter surface.

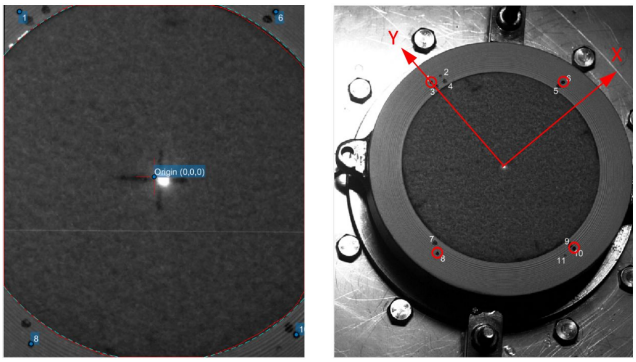

Fig. 3. Crosshair (left) and arrows (right) define origin and orientation of used camera pose-independent right-handed reference coordinate system. For calibration purposes, 11 dedicated reference points with known world coordinates on the filter fixing ring were defined (right). Red circles (right) respectively blue dots (left) mark the selected reference point subset during calibration routine – in particular case marker 1, 6, 8 and 10.

D. Annotation of Patches

The segmentation of individual filter cake patches is crucial to further assess their geometric parameters and temporal evolution (i.e. motion, further splits, collisions, etc.). A fully automated procedure is not deemed feasible, because it is a subjective measure when an individual fragment is completely detached from its neighbors, and how to assess partially occluded fragments. In addition, the visibility of patches may be affected by dust, and tilted stains may have a shaded surface that slowly fades into the black background. Therefore, AnnotationAssistant (an interactive segmentation software) has been designed for annotating patches semi-manually. The program takes a dataset of rectified images and let you select a specific image or step through the recorded image sequence. Fragments are annotated by marking a contour polygon. The process is assisted by an edge refinement between marked polygon points. Hereby, the connecting line between labeled polygon points is adapted to follow the local edges inbetween. Once annotated, filter cake fragments can be investigated based on automatically calculated geometric features. Figure 4 shows the first image where filter cake detachment initiates.

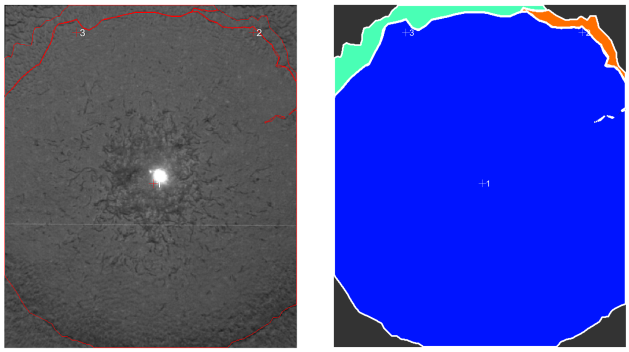

Fig. 4. First frame in recorded sequence showing the beginning of filter cake detachment. The left image shows annotated patches in this frame, gathered with the aid of AnnotationAssistant. The right image depicts the related label mask. Patch boundaries are schown in red.

Manual annotation is feasible for patches with length of at least 2 *mm*. Each patch automatically receives a unique identifier and is stored in a database. It can be refined and edited later on. For efficiency, labeled patches can be copied to the next time frame to be edited and adjusted to the new patch positions.

E. Extraction of Tracked Positions

In order to create consistent trajectories for segmented patches, they need to be tracked over time. Also here, automated approaches are deemed infeasible, as the patch motion between frames may be up to 20° in rotation and a quarter of the image area in translation. The appearance of a patch can change drastically between images, so local vicinity constraints cannot be applied. Rotation of patches in particular brings considerable appearance changes, so an explicit matching based on surface shape or contour is not feasible either.

The inroduced interactive AnnotationAssistant in Section III-D calculates geometric parameters and statistics, which are gathered per patch and allow quantitativ evaluation of the filter cake detatchment process. These parameters comprise patch center of gravity position, covered area, perimeter, orientation, several depth measures (real world z-position of a patch relative to filter fixation ring center) as well as the surface normal vector as a result of a plane fitting routine conducted on the 3D point cloud and some more statistics.

F. Distance from Filter Plane

The Z coordinates for an evaluated image can be seen in the corrected depth map on the right side of Figure 5. To obtain the course of detached patches, the image sequences are reduced to relevant ones that represent the detachment process. Patches may emerge, break into smaller patches, merge again or leave the observation window. The evolution of the patches can be represented, for example, in the form of a dendrogram, where the branch length represents the image sequence. Including the patch position, the paths of all patches can be ploted in a single, 3D space representing graph which requires renumbered patches [1].

IV. Experimental Results

In this chapter the quality of the measured geometric features of tracked patches is analyzed. First, the accuracy of the depth delivered by the application is determined. Then, limitations of reliability are indicated for certain conditions during cleaning. Finally, the propagation of the patches in Z direction is plotted and the degree of regeneration is calculated. Confidence intervals are given for 95% significance.

A. Depth Accuracy Considerations

Considering a surface resolution of $86-90\ \mu m/px$ and a depth to baseline ratio of $4:1$, a stereo matching accuracy of $\pm 0.5px$ will translate to a depth error of ± 0.18 *mm*. Compared to the theoretical accuracy obtained by stereo-optic algorithms, the accuracy reachable in practice is lower, due to surface roughness and porous structure of filter fibers. The metallic surface of the ring reflects a good coordinate transform to the filter plane in the figures that follow. This plane may be tilted slightly, if the calibration points chosen at the markers differ in notch depth. For a fresh filter placed flat in the holder and fixed tightly, there is outward bulging as in Figure 5. The metal surface fluctuates in the range of -0.059 to 0.597 *mm*. Because of indented markers the true filter plane lies at a mean depth of 0.227 ± 0.041 *mm*. Near the center the fresh filter, i.e., a needle felt of untreated surface, fluctuates between 1.06 and 1.38 *mm*, a considerable surface roughness.

However, after filtration the deposited particulate layer differs radially in height as shown in Figure 6. The particulate surface on top of the metal ring is 0.19 to 0.785 *mm* away from the calibrated filter plane, which fluctuates in the same range as before, without particulate layer. The mean depth from the filter plane at the metal ring is 0.55 ± 0.047 *mm*. So the particulate layer adds 0.323 ± 0.064 *mm* thickness on top of the true filter plane. Layers on top of the metal ring may inherit the imperfections from the metal ring. On top of the filter far away from its circular edge and unintentionally created crater at center (due to large filtration velocity), the particulate surface fluctuates between 1.6 and 1.95 *mm* as a measure for surface roughness. Averaging over the regarding areas along the profile could smoothen the respective areas on top of the filter ranging from 1.63 to 1.85 *mm* in depth.

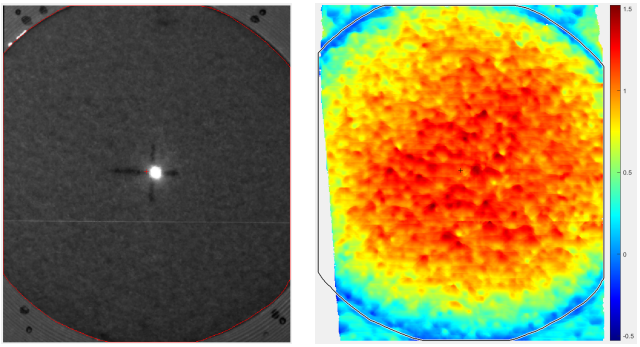

Fig. 5. Left: Image of a fresh, particle-free, flat clamped filter. The reference filter area is outlined red. Black dots represent reference markers. Right: Corrected auto-scaled depth map of the fresh filter area in *mm*. As can be seen, the filter bulges out.

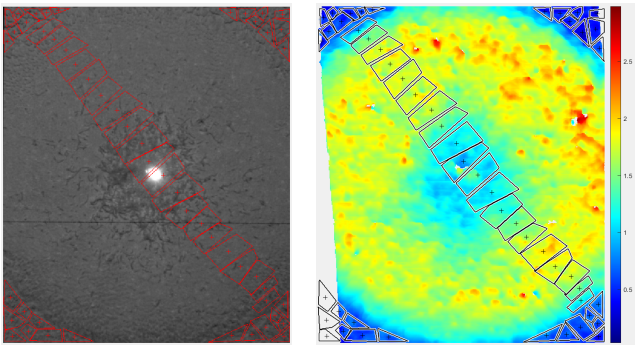

Fig. 6. Depth of particulate layer after filtration, in auto-scaled mm (right). Annotations for top of metal ring and radial profile (red outlines). See the fluctuations beside a radial distribution.

The flattest surface is on top of the metal ring; therefore, the accuracy of depth is 0.094 *mm* and may change for the thickness, here 0.128 *mm* (confidence width).

B. Limitations of Observation

Detachment of particulate matter is indicated in the first instance by breakups on (and in) the surface. Onsets of cracks on a surface are hard to detect, humans may assess from later crack propagation. Figure 7 shows the first breakup on the surface that later leads to patch detachment. More breakups occurred before a patch liberated from the filter surface. For comparison reasons the depth scale was manually set to the same range as in Figure 7 to Figure 10.

Liberated patches obey gravity but move to the top of the image as in Figure 7 due to test rig misplacement where the right side became the bottom side in this exemplary experiment. The cameras and so the images kept their relative

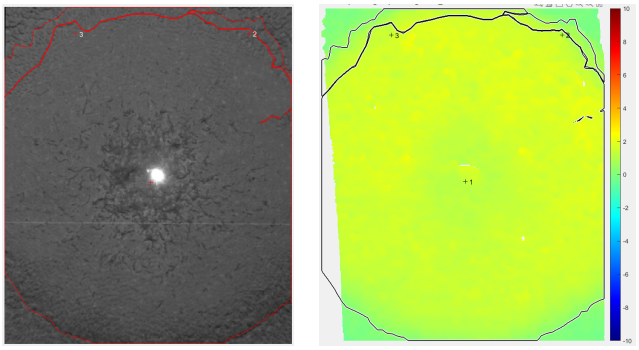

Fig. 7. Depth map at onset of detachment, in mm (right). Numbered patches (red outlines). Figure out surface cracks and see the point markings outside of concave patches 2 and 3.

position. The patches rotate and do not have sharp edges, a human may regard areas subjectively as patches or not, as is shown. Patches overlay each other and tilt at the surface. Sharp jumps in distance cause stereo-matching to fail. For instance, a projection of a distant object is clear at one viewing angle but the projection of the same object from a different viewing angle hides a spot seen with the former viewing angle where stereo-matching fails. It may wrongly produce a counter-copy for large distant objects of inverse increased distance like the blue one at the bottom right half.

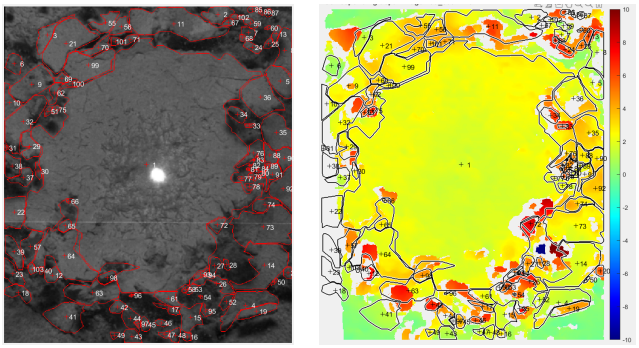

Fig. 8. Annotated and numberated patches at end of liberation process (left) and corresponding depth map based on mm (right).

The mismatch may be clearer from an example of the two viewing angles. At the left half of Figure 9 there may be an object within the blue rectangle. At the right half the scene is viewed from an angle at the right and the object captured within the blue rectangle. The position of the object differs in both images, where the depth at the image position of the back camera seems to be correct and the counter-copy is situated at the image position of the front camera. A small, resolved particle causes the stereo-matching to fail as well, highlighted are areas with numerous closely resolved particles. Smaller, unresolved particles may smear within a pixel to altered brightness and color.

Patch 6 at the top left is surrounded by particles so small (1-3 pixels) that one may interpret that as fog of dust. At this intermediate condition stereo-matching fails at some locations of the dust. If the objects are smaller, they blur the

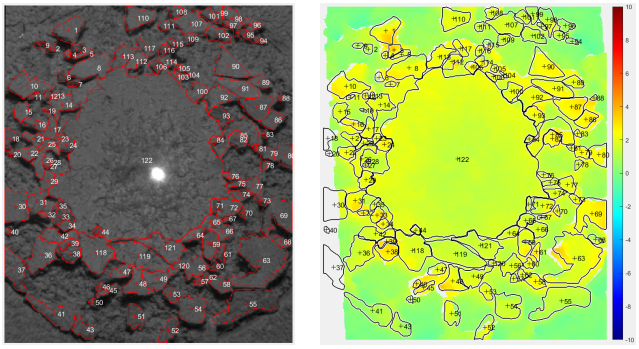

Fig. 9. Depth map at the end of cleaning, in mm (right). From camera view, gravity goes up. Numbered patches (red outlines).

background and stereo-matching generates the background depth, not shown here. An event of a dense haze of dust was not found, therefore it is not clear so far whether stereo-matching can cope with haze. Matched surfaces are subject to little random fluctuations among an image sequence.

C. Degree of Regeneration Analysis

At the end of cleaning, patches have either completely detached from the filter surface, have remained at their place or redeposited at the surface. An example is shown in Figure 10. In a conservative (safe assumption) view of non-regenerated area, tilted patches are considered by their unprojected surface area and areas of covering patches are considered multiple times. Those small areas were neglected where a normal vector was not provided.

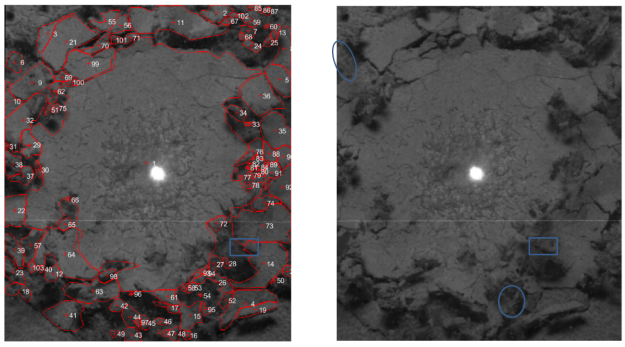

Fig. 10. Stereo images of back (left) and front (right) camera at end of detatchment process. From camera view, gravity goes up. All annotated patches are numbered (red outlines, left). Blue rectangles denote examples of tilted patches that lead to false area results and blue ellipses mark examples of small particles.

The degree of regeneration is the ratio of liberated quantity to initial quantity, here quantified by area. Using projected areas alone gives 39.8% [1]. The conservative approach gives 20.2%.

D. Patch Trajectory Analysis

To plot the distance that the patches travelled the individual patches are abstracted in Figure 11 by their projected radial position from the filter center. The individual patch areas are indicated by the size of the circles. To ascertain a

trend a few consecutive images were selected. During the cleaning air pulse, the filter moves from the initial stage (image 000000) to the final stage (image 004002), where the radial profile of the surface was obtained from the deposited patches. This reflects the crater of almost no dust at the center and the bulge caused by the pulse of pressurized air. Strictly speaking, the measurements are from the top of the patches. Compared with Figure 10 the circumference at about 20*mm* is mostly of tilted patches with larger surface dimensions than thickness. Therefore, the radial profile fit to their mean depths overestimates the filter surface more than the fit to mean depths of plane patches. The patch at the center is the largest occupying a radius of 11*mm* the least as other patches appear at larger radii. Some of them may have redeposited on top of the central patch which requires further investigation. Prior to image 000219 the large patches have existed since the detachment. Over the course of a patch movement, it may appear in the selected images for a short while and disappear from the plot. As filtration was discontinued during cleaning, the patches experience only the force exerted by the compressed air on the filter and follow that path afterwards (up arrow). For this experiment the test rig was placed with the right side at the bottom, therefore the filter is oriented vertically and gravity acts on the patches laterally to the filter plane. Thus, the particles follow a rather parabolic path in the plot. The pulse lasted longer than the images were captured. However, one patch seems to redeposit (down arrow), outside the filter.

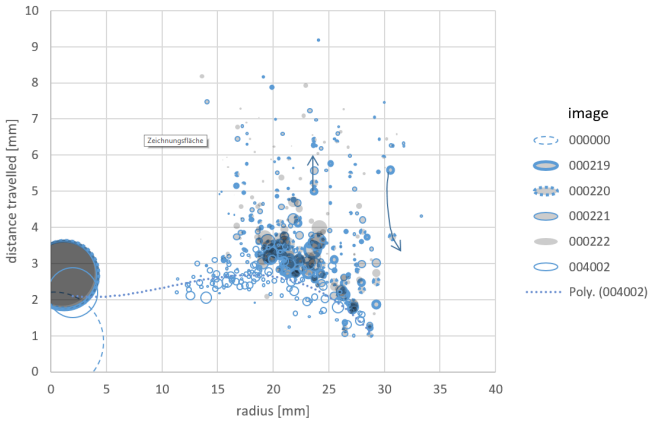

Fig. 11. Travelled distance between 22^{nd} and 28^{th}*ms* of detachment (000219 to 000222, grey of various outline) against radius from filter center, plus initial (000000 of dashed outline) and final stage (004002 of solid outline). Circle size indicates patch area. Final surface (dotted trendline); at final stage all shown patches are deposited on filter.

V. Conclusions

In total, 77 experiments have been conducted, with the filter cleaning process captured on a series of 15 to 20 images per experiment. The presented computer vision setup and analysis system allows for the first time a quantitative, three-dimensional analysis of dust filter cleaning processes at 500 *Hz*. It is evident, that errors in size and orientation of patches can occur on an individual level due to mismatches and due to the patch shape. Typically, patches have an area of 5 $mm \times 5$ *mm*, with a thickness smaller than 2 *mm*. If a patch rotates and is viewed from the side, its size will be grossly underestimated. The last Figure 10 shows that it is possible to distinguish between redeposited patches and patches that remain at the filter at a size-based level.

VI. Outlook

As a result of this work, the cumulative area distributions can be obtained from the experiments and will be compared with data from literature. Also, the validation of simulations will become possible in terms of motion paths of the patches, and velocities of the patches at a given time, as soon as above measures allow error-tolerant tracking of individual patches. Based on this data set, the next step is to create evolution-trees of patches, i.e. to track the decomposition of patches into smaller ones and establish relationships to ancestors and predecessors. To identify the class of patches that travel long distances, more cumulative analyses will assist, in terms of their size and local origin. The labeled dataset of fragments will act as a reference in the future to train an automated instance segmentation, where the now laborious patch labeling will be replaced by a per-pixel classification step. In occluded regions, where the matching of two cameras failed, additional cameras may assist, i.e., a multi-camera-view, especially in the matching of layered objects. Besides the tracking of patches, by the above measures, the local and time-resolved investigation of powdery layer breakage may become possible. Finally, the movement of flexible filters or the compaction of powder layer may be determined separately.

References

[1] V. D'Ercole, "Study of movement and dimension of filter cake patches during pulse jet cleaning by high-speed stereo camera for identifying optimal cleaning conditions," Master's thesis, Graz University of Technology, 2021.

[2] A. Dittler, B. Gutmann, R. Lichtenberger, H. Weber, and G. Kasper, "Optical in situ measurement of dust cake thickness distributions on rigid filter media for gas cleaning," *Powder Technology*, no. 99, pp. pp. 177–184, 1998.

[3] H. Hirschmüller, "Semi-global matching – motivation, developments and applications," *Photogrammetric Week*, 2011.

[4] C. Kanaoka and M. Amornkitbamrung, "Effect of filter permeability on the release of captured dust from a rigid ceramic filter surface," *Powder Technology*, vol. 118, pp. 113–120, 2001.

[5] M. Klopschitz, G. Lodron, G. Paar, and B. Huber, "Line processes for highly accurate geometric camera calibration," in *Proc. AAPR*, 2017.

[6] F. Löffler, H. Dietrich, and W. Flatt, *Dust Collection with Bag Filters and Envelope Filters*, H. Simon, Ed. Springer Fachmedien Wiesbaden, 1988.

[7] M. Rüther, M. Saleem, H. Bischof, and G. Krammer, "In-situ measurement of dust deposition on bag filters using stereo vision and non-rigid registration," *Assembly Automation*, vol. 25, no. 3, pp. 196–203, 2005.

[8] M. Rüther, M. Uray, H. Bischof, G. Krammer, and M. Saleem, "An optical measurement device for evaluating dust deposition on flexible filter surfaces," in *10th Computer Vision Winter Workshop CVWW 2005*, 2005.

[9] G. Yang, J. Manela, M. Happold, and D. Ramanan, "Hierarchical deep stereo matching on high-resolution images," in *2019 IEEE/CVF Conference on Computer Vision and Pattern Recognition (CVPR)*, 2019.

[10] Z. Zhang, "A flexible new technique for camera calibration," *IEEE transaction on pattern analysis and machine intelligence*, vol. 22, no. 11, pp. 1330–1334, 2000.